Nano-Micro Letters
e-ISSN 2150-5551
CN 31-2103/TB
ARTICLE
https://doi.org/10.1007/s40820-026-02224-6

Cite as
Nano-Micro Lett.
(2026) 18:391

Received: 7 January 2026
Accepted: 17 April 2026

Controlled Epitaxial Growth of Perovskite Single-Crystal Heterojunction Arrays for Self-Powered Imaging

Hui Lu[1,2,3], Yang Yu[1], Wenqiang Wu[2] ✉, Zeping He[1,2,3], Kaiyu Hu[2], Wenqiang Yang[2], Xun Han[2,4] ✉, Caofeng Pan[1,2,3] ✉

HIGHLIGHTS

- A versatile selective epitaxial growth strategy was developed for fabricating perovskite single-crystal heterojunction arrays, enabling precise control over pixel size, arrangement angle, and crystal orientation.
- The self-powered photodetector arrays based on the single-crystal heterojunction exhibited high sensitivity with a weak-light detection limit of 9 nW cm^{-2}, long-term operational stability, and clear imaging capability under zero bias.

ABSTRACT Perovskite single-crystal heterojunction arrays exhibit significant application potential in advanced optoelectronics, however, achieving comprehensive control over crystallographic and spatial properties of the array remains challenging. Here, we report a selective epitaxial growth strategy for fabricating single-crystal $MAPbCl_3$/$MAPbBr_3$ and $MAPbBr_3$/$MAPbI_3$ heterojunction arrays. This method employs patterned polymer templates to define the pixel dimension and arrangement, while the underlying single-crystal substrate guides the crystal orientation of the heterojunction array, enabling precise control over the pixel size, pixel arrangement angle and crystal plane. The self-powered photodetector arrays were fabricated based on these heterojunctions, showing a specific detectivity of 6.0×10^{11} Jones, a weak-light detection limit of 9 nW cm^{-2} and long-term operation stability under zero bias. Furthermore, the light pattern with different illumination intensities could be clearly imaged by the device array in the self-powered mode. This work establishes a robust method of fabricating the single-crystal heterojunction arrays for advanced optoelectronic applications.

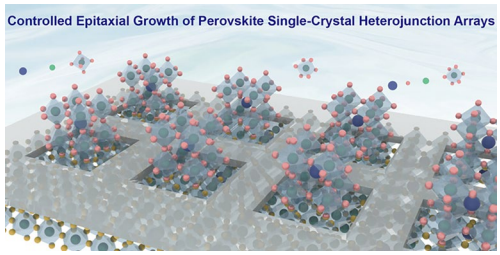

KEYWORDS Perovskite single crystals; Heterojunction arrays; Selective epitaxial growth; Orientation control; Self-powered imaging

1 Introduction

Metal halide perovskites have emerged as highly promising materials for optoelectronic applications, including solar cells [1–6], light-emitting diodes [7–12], photodetectors [13–21], lasers [22–27], and neuromorphic devices [28–33]. The perovskite single crystals exhibit low trap-state densities, high carrier mobilities, and enhanced intrinsic stability compared to the polycrystalline perovskite films [34–37]. These properties make them an ideal platform for the

Hui Lu and Yang Yu have contributed equally to this work.

✉ Wenqiang Wu, wuwenqiang@buaa.edu.cn; Xun Han, xunhan@buaa.edu.cn; Caofeng Pan, pancaofeng@buaa.edu.cn
[1] CAS Center for Excellence in Nanoscience, Beijing Key Laboratory of Micro-Nano Energy and Sensor, Beijing Institute of Nanoenergy and Nanosystems, Chinese Academy of Sciences, Beijing 101400, People's Republic of China
[2] Beijing Key Laboratory for Atomic Manufacturing Equipment and Intelligent Sensing, Institute of Atomic Manufacturing, Beihang University, Beijing 100191, People's Republic of China
[3] School of Nanoscience and Technology, University of Chinese Academy of Sciences, Beijing 100049, People's Republic of China
[4] Department of Applied Physics, The Hong Kong Polytechnic University, Hong Kong 999077, People's Republic of China

Published online: 29 May 2026

high-performance optoelectronic devices. For the advanced applications, such as the high-resolution imaging, display and integrated optical systems, the fabrication of the perovskite single crystal into ordered array is highly required [13, 16, 20, 38–40]. Furthermore, creating single-crystal heterojunctions by interfacing two different perovskite materials is a critical step for endowing new functions and enhancing device performances [41–44]. The engineered band alignment at the interface can create the built-in electric field, which could facilitate efficient charge separation and enable self-powered optoelectronic devices [45–47].

Numerous progress has been made for the fabrication of the heterojunctions on bulk crystals or in layered films, such as utilizing the type-I band arrangement formed by quasi-2D perovskite and 3D perovskite to improve the luminous efficiency of LEDs and using partial ion exchange to prepare transverse heterojunctions with different halogen components in the type-II band alignment to improve the response capability of photodetectors [48–53]. However, the fabrication of large-scale heterojunction arrays of perovskite single crystals has not been explored. This is due to the gap between the bulk fabrication and array integration of the heterojunction, which requires miniaturizing and spatially confining the liquid-phase heterojunction formation process to construct discrete and uniform small pixels with desired pattern. Moreover, there is lack of crystallographic control methods across the heterojunction array, which often results in randomly oriented crystals, leading to severe pixel-to-pixel variations. Therefore, a method that ensures every single heterojunction pixel maintains the same orientation is urgently needed.

Here, we introduced a selective epitaxial growth approach for the perovskite single-crystal heterojunction arrays. This approach utilizes a patterned polymer template to precisely define the patterns for heterojunction formation, while arranging the crystal orientation of the entire heterojunction array to be coherently locked to that of the epitaxial substrate. Based on this strategy, the $MAPbCl_3/MAPbBr_3$ and $MAPbBr_3/MAPbI_3$ single-crystal heterojunction arrays were fabricated with precise control over pixel size, pixel angle, and crystal orientation. Vertically aligned perovskite single-crystal heterojunction photodetector arrays were further demonstrated, showing a weak-light detection limit of 9 nW cm^{-2} and a high specific detectivity of 6.0×10^{11} Jones at 0 V bias. Due to the uniform pixel photoresponse, the device exhibited clear pattern imaging capabilities across varying light intensities in the self-powered mode. This work provides a simple method for heterogeneous integration of perovskite single crystal arrays toward the high-performance optoelectronic devices.

2 Experimental Section

2.1 Materials

N,N-Dimethylformamide (DMF) (99%), dimethyl sulfoxide (DMSO) (99%), γ-butyrolactone (GBL) (99.9%), dipropyl sulfoxide imide (DPSI) (99.9%), methylammonium iodide (99.99%), lead iodide (99.9%), lead bromide (99.9%), lead chloride (99.9%), acetone (99%), and anhydrous ethanol (99.9%) were purchased from Aladdin Scientific. All commercial products were used inside a nitrogen-filled glove box.

2.2 Fabrication of the Self-powered Photodetector Arrays

The fabrication of self-powered perovskite photodetector arrays based on $MAPbCl_3/MAPbBr_3$ and $MAPbBr_3/MAPbI_3$ heterojunctions was initiated by synthesizing $MAPbCl_3$ and $MAPbBr_3$ single crystals through a spatial confinement growth method and temperature-programmed crystallization from their respective precursor solutions dissolved in DMF/DMSO and DMF. Subsequently, a patterned Parylene-C template with selectively exposed regions was fabricated on the substrate via sequential coating, photolithography, and dry etching processes. Heteroepitaxial growth was then performed within these openings: the $MAPbCl_3/MAPbBr_3$ heterojunction was fabricated by growing $MAPbBr_3$ crystals via solution epitaxy from a $MAPbBr_3$-DMF precursor, whereas the $MAPbBr_3/MAPbI_3$ heterojunction was formed by epitaxially growing $MAPbI_3$ crystals from a $MAPbI_3$-GBL precursor. Finally, the device integration was completed by depositing electrode arrays through thermal evaporation with a shadow mask, enabling the realization of self-powered photodetector arrays.

https://doi.org/10.1007/s40820-026-02224-6

3 Results and Discussion

3.1 Selective Epitaxial Growth of Perovskite Single-Crystal Heterojunction Arrays

The fabrication process for the patterned perovskite single-crystal heterojunction arrays is schematically illustrated in Fig. 1a. The process begins with the growth of single-crystal perovskite films on indium tin oxide (ITO) glass via a spatial confinement method, which serve as the substrates for subsequent epitaxial growth. Then, a thin Parylene-C film is deposited and patterned on the single-crystal perovskite substrate, creating openings with defined positions and sizes for the crystal epitaxial growth. Finally, the ordered single-crystal heterojunction array is formed in the openings of the Parylene-C film through the selective epitaxial growth. A more detailed fabrication process can be found in Fig. S1 and the Experimental section. Two different heterojunction arrays were fabricated, including the methylammonium lead iodide on a bromide substrate ($MAPbBr_3/MAPbI_3$) and methylammonium lead bromide on a chloride substrate ($MAPbCl_3/MAPbBr_3$). The selective epitaxial growth on the perovskite substrate involves the three stages which are different from those for the growth of a continuous perovskite film, typically involving precursor supersaturation, nucleation, and crystal growth (Fig. S2). For the selective epitaxial growth of the array, upon introduction of the precursor solution, halide ion exchange occurs in the surface region of the substrate exposed within the Parylene-C film openings. This creates a graded transition layer, such as the $MAPbI_{3x}Br_{3(1-x)}$ film on the $MAPbBr_3$ surface, which also facilitates lattice-matched nucleation and homoepitaxial growth of the target $MAPbBr_3$ arrays (Fig. 1b). The epitaxial growth of $MAPbI_3$ on $MAPbBr_3$ is achieved along the [1 0 0] crystal direction. Notably, nucleation occurs uniformly for those continuous thin films, but preferentially along crystal edges for ordered $MAPbI_3$ arrays (Fig. S3). This selective epitaxial growth enables the fabrication of large-scale and high-density single-crystal arrays. Figure 1c shows a scanning electron microscopy (SEM) image of a large-scale $MAPbI_3/MAPbBr_3$ single-crystal heterostructure array, which exhibits a highly ordered and uniform arrangement array, comprising 44×44 individual heterojunctions within a 1.5×1.5 mm^2 area. Similarly, the $MAPbCl_3/MAPbBr_3$ single-crystal heterojunction arrays were fabricated, demonstrating the uniform orientation and size as well as the sharp edges of the individual pixel (Fig. 1d). To investigate the structure and elemental distribution of the heterojunction arrays, the energy-dispersive spectroscopy (EDS) elemental mapping was performed. As shown in Fig. 1e, Cl is mainly distributed in the bottom substrate layer and Br is confined to the top epitaxial layer, while Pb demonstrates a homogeneous distribution throughout the entire structure. A line scan across the heterojunction confirms the element distribution (Fig. 1f). The concentrations of Cl and Br change gradually across the heterojunction, forming a graded transition region with a width of approximately 4 μm. This wide and graded junction confirms the initial ion-exchange process before the bulk crystal growth in Fig. S2. Similar compositional grading was also observed in the $MAPbBr_3/MAPbI_3$ heterojunction (Fig. S4).

3.2 Epitaxial Growth Dynamics of Perovskite Single-Crystal Heterojunctions

To elucidate the epitaxial growth dynamics, the epitaxial growth of the $MAPbBr_3$ on the $MAPbCl_3$ substrate was investigated. $MAPbCl_3/MAPbBr_3$ perovskite heterojunctions were prepared via a saturation concentration liquid-phase epitaxial growth in the heated $MAPbBr_3$ precursor solution (Fig. 2a). Before the epitaxial process, $MAPbCl_3$ crystals, utilized as the substrate, are obtained using a spatial confinement method liquid-phase diffusion crystallization process. The X-ray diffraction (XRD) pattern of the $MAPbCl_3$ substrate displays a series of strong (100), (200), and (300) peaks, indicating the cubic phase with a preferred orientation along the $<100>$ direction (Figure. 2b). The inset SAED (selected area electron diffraction) pattern further confirms the single-crystal properties of the substrate. The emission and absorption properties of $MAPbCl_3$ substrate were also investigated (Fig. 2c). The photoluminescence (PL) peak is centered at 405 nm and the absorption band edge is at 3.02 eV. The charge-carrier dynamics of the $MAPbCl_3$ single crystal was analyzed by time-resolved PL (TRPL) spectroscopy. The TRPL decay curve is fitted with a double-exponential fitting model with a fast decay time and a slow decay time of 1.43 and 36.53 ns, respectively (Fig. 2d). The fast decay process is caused by the bimolecular recombination of photogenerated free carriers, whereas the slow decay process is attributed mainly to trap-assisted

recombination. These properties confirm the high-quality of the $MAPbCl_3$ single crystal substrate.

The evolution of the heterojunction formation was monitored by tracking the PL emission of the sample at different growth intervals. As shown in Fig. 2e, a systematic redshift of the PL peak is observed as the growth time increases from 5 to 35 s. This redshift is consistent with a halide exchange process, leading to the formation of mixed halide perovskites with progressively increasing Br content. To avoid the formation of stray crystals and obtain high-quality heterojunctions, the epitaxial growth rate was optimized by maintaining the crystallization temperature within a narrow range of 100 to 110 °C. The $MAPbBr_3$ arrays can be observed after about 1 min of epitaxial growth. The average sizes of the individual pixels with the growth time under different growth temperatures are summarized in Fig. 2f. The pixel size increases with growth time at both temperatures, eventually reaching and slightly exceeding the Parylene-C opening size of 20 μm. Furthermore, a higher temperature can accelerate the growth rate, leading to a larger pixel size compared to the growth at a lower temperature over the same period. Similar growth processes were also observed

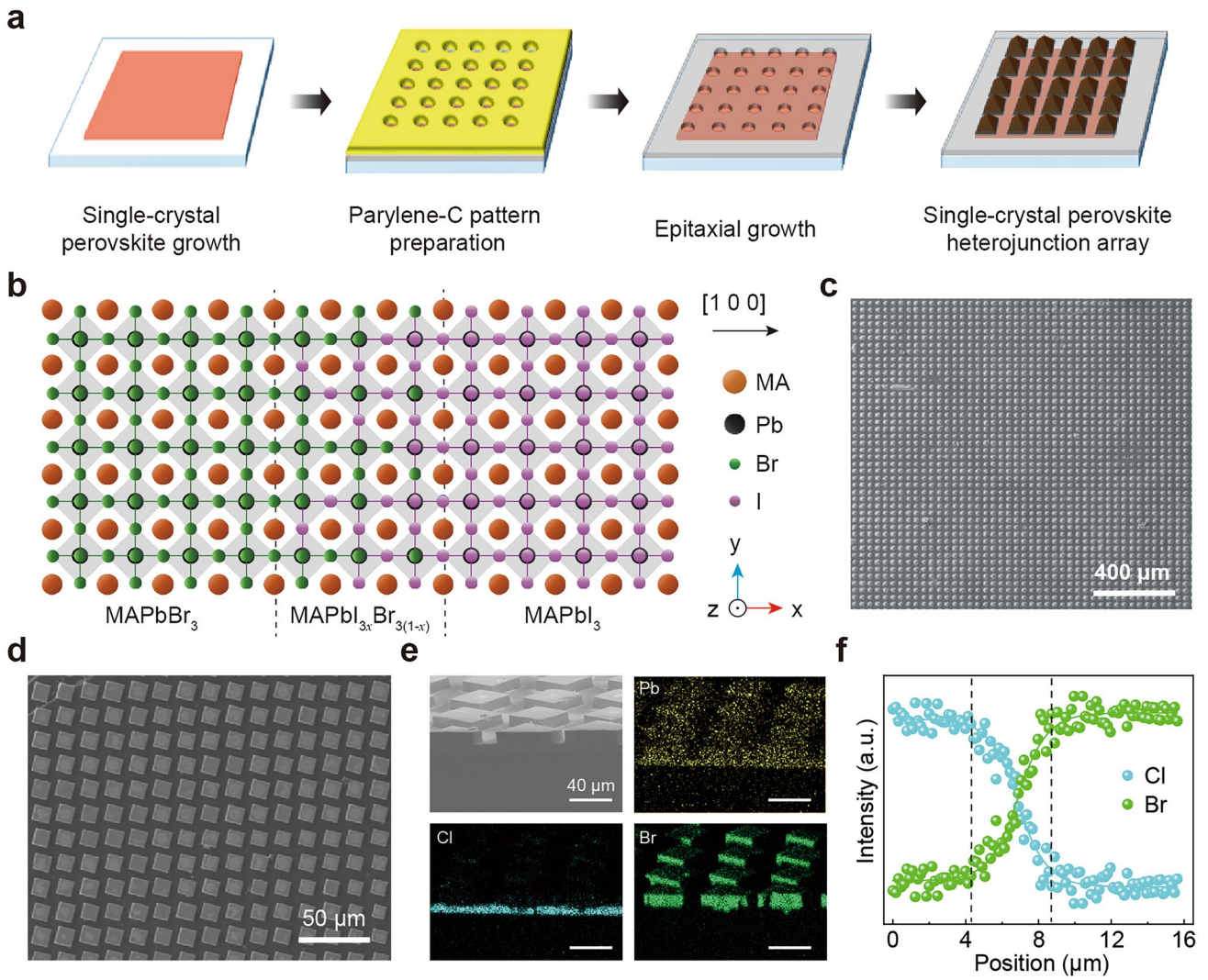

Fig. 1 Schematic illustration of selective epitaxial growth of perovskite single-crystal heterojunction arrays. **a** Schematic of the fabrication process for the patterned perovskite single-crystal heterojunction arrays. **b** Mechanism of epitaxial growth of perovskite single-crystal heterojunction arrays. **c** Schematic diagram of the ideal lattice-matched epitaxy between $MAPbBr_3$/$MAPbI_3$ along the [100] crystallographic direction. **d** SEM image of a large-scale $MAPbBr_3$/$MAPbI_3$ single-crystal heterojunction array (44 × 44 array). **e** SEM image of $MAPbCl_3$/$MAPbBr_3$ single-crystal heterojunction array and EDS map of the $MAPbCl_3$/$MAPbBr_3$ single-crystal heterojunction array. **f** Distribution of halogen elements across the $MAPbCl_3$/$MAPbBr_3$ single-crystal heterojunction

https://doi.org/10.1007/s40820-026-02224-6

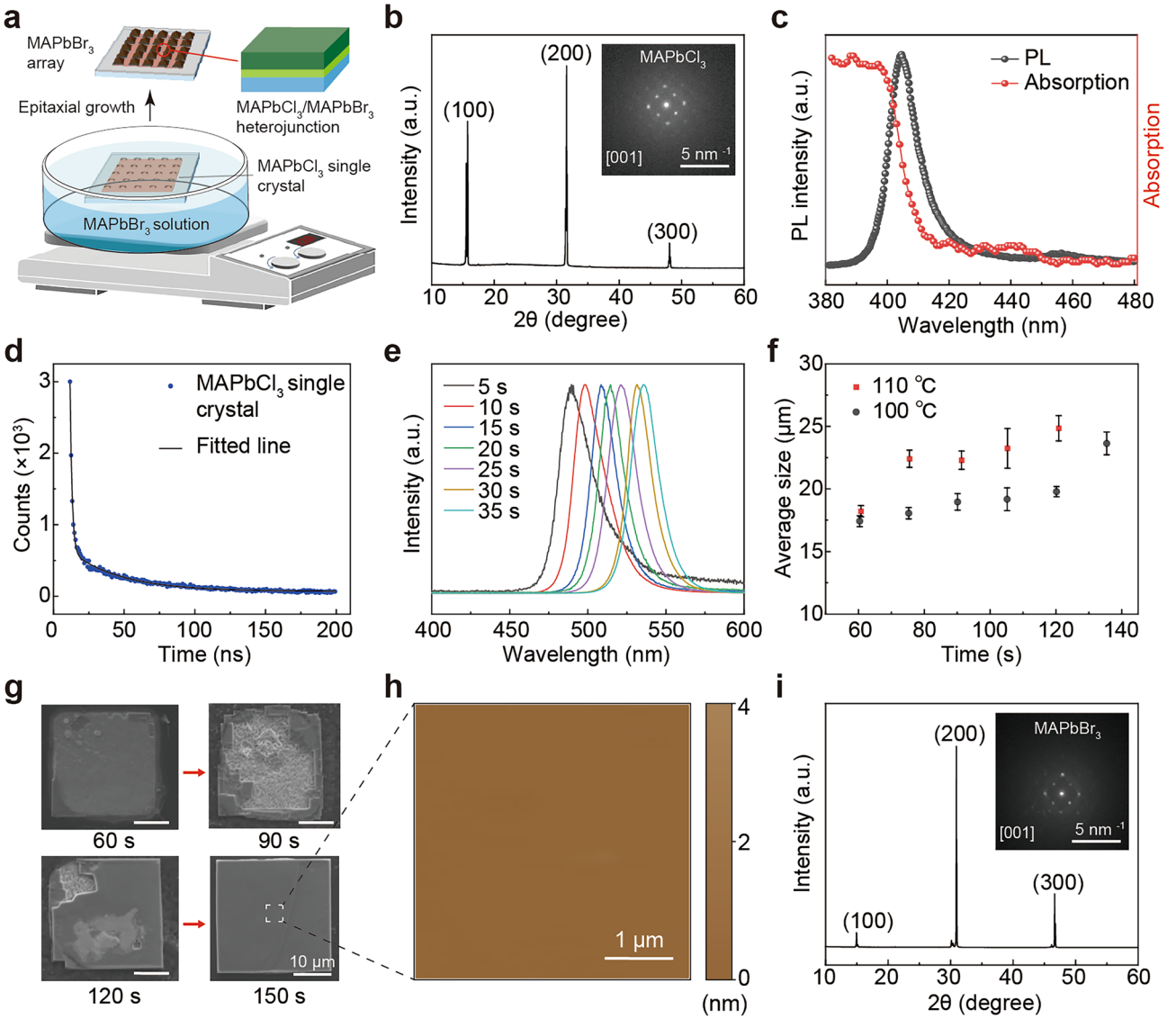

Fig. 2 Growth dynamics of $MAPbCl_3/MAPbBr_3$ perovskite single-crystal heterojunction arrays. **a** Schematic of the experimental setup for $MAPbCl_3/MAPbBr_3$ perovskite single-crystal heterojunction arrays. **b** XRD pattern of $MAPbCl_3$ single crystal substrate. Inset: SAED pattern. **c** PL and absorption spectra of $MAPbCl_3$ single crystal substrate. **d** TRPL decay curve of $MAPbCl_3$ single crystal substrate. **e** PL spectra of $MAPbCl_3/MAPbBr_3$ perovskite single-crystal heterojunction at different growth durations. **f** Average array size versus growth temperature and duration. **g** SEM images of epitaxial $MAPbBr_3$ perovskite grown at different durations. **h** AFM image of an epitaxial $MAPbBr_3$ single crystal pixel. **i** XRD pattern of the epitaxial $MAPbBr_3$ single crystal array. Inset: SAED pattern

for the $MAPbBr_3/MAPbI_3$ heterojunction arrays (Fig. S5). Figure 2g demonstrates the morphological evolution of an individual $MAPbBr_3$ perovskite crystal pixel in $MAPbCl_3/MAPbBr_3$ heterojunction arrays under 110 °C conditions. Initially, the small crystallites nucleate within the opening and after 150 s, they fully merge into a square pixel with sharp edges and a flat surface. An atomic force microscopy (AFM) image of a $MAPbBr_3$ perovskite pixel confirms the smooth surface morphology, with a roughness of 2.082 nm in a 20×20 μm^2 area (Fig. 2h). The crystal structure of the epitaxial $MAPbBr_3$ perovskite array was characterized by XRD analysis. As shown in Fig. 2i, the XRD pattern of the $MAPbBr_3$ perovskite array also demonstrates the strong diffraction peaks of (100), (200), and (300) and the SAED patterns along the [001] zone axis further confirms the high crystallinity and cubic phase of the $MAPbBr_3$ perovskite

array. During the transition from $MAPbCl_3$ to $MAPbBr_3$, the primary change is the expansion of the lattice parameter due to the larger ionic radius of Br^- compared to Cl^-. This results in a shift of the XRD diffraction peaks toward lower 2θ values, consistent with Bragg's law (Fig. 2i). The SAED pattern of the epitaxial $MAPbBr_3$ array along the [001] direction is similar to that of the $MAPbCl_3$ substrate, indicating that the crystal symmetry is preserved during the halogen substitution.

3.3 Regulation of Geometric and Crystallographic Properties of Epitaxial Perovskite Single-Crystal Arrays

The selective epitaxial growth method demonstrates versatile control over the geometric and crystallographic properties of the epitaxial perovskite arrays, including the precise regulation of the pixel dimensions, pixel arrangement angle and crystal orientation. The dimensions of the individual single-crystal pixels are highly dependent on the size of the openings in the Parylene-C film under a certain epitaxial growth condition. As shown in Fig. 3a, uniform $MAPbI_3$ arrays with different predefined pixel dimensions were fabricated on the $MAPbBr_3$ substrate. We statistically analyzed the dimensions of the 100 individual pixels for each Parylene-C opening size. The average width of the pixel exhibits a strong linear relationship with the Parylene-C opening size and the narrow width distribution for each set, indicating the excellent uniformity of the array (Fig. 3b). Furthermore, the width of the pixel is usually larger than the corresponding openings. For example, the openings of 30 μm generated pixels with an average size of about 45 μm, ensuring 100% coverage for each pixel. The rotational alignment of the entire array can be controlled by tuning the angle between the patterned openings and the crystallographic axes of the substrate (Fig. 3c). The $MAPbI_3$ arrays with the openings rotated at 0° and 45° relative to the crystal directions of the substrate were fabricated. As shown in Fig. 3d, e the $MAPbI_3$ pixels demonstrate a clear rotation with the angle of 45°, which precisely replicates the opening's rotational alignment. In addition to the external geometric control, the crystal orientation of the array can be modified by introducing additives or using different substrate surfaces due to the lattice matching. The addition of DPSI to the precursor solution modifies the crystal habit of $MAPbI_3$ arrays, promoting the exposure of the (100) facets rather than the (110) facets. The size control was also maintained during this process (Fig. 3f). Figure 3g shows the morphology of the epitaxial perovskite arrays with DPSI, transforming from the pyramidal shape to a cubic. Importantly, the SAED patterns of the substrate (Fig. 3h) and the epitaxial perovskite arrays with DPSI (Fig. 3i) show a consistent crystal orientation, confirming that the epitaxial relationship is preserved despite the change in crystal habit. Moreover, by utilizing $MAPbBr_3$ substrates with different surface orientations, such as (111) and (110), both the morphologies and orientations of the $MAPbI_3$ arrays can be directly changed correspondingly. As shown in Fig. 3j, k the pixel shapes changed to be consistent with the substrate orientations. This selective epitaxial growth method also demonstrated the controllability over the size, rotation and orientation of the $MAPbBr_3$ arrays on the $MAPbCl_3$ substrate (Figs. S6-S8), highlighting the capability of this method for controllable fabrication of single crystal perovskite arrays.

3.4 Characterization of the Self-Powered Photodetectors Based on Perovskite Single-Crystal Heterojunction Arrays

Self-powered photodetector arrays (8 × 8 pixels) based on both $MAPbBr_3/MAPbI_3$ and $MAPbCl_3/MAPbBr_3$ heterojunction arrays were fabricated through the deposition of the patterned metal electrodes on the heterojunctions. Based on the absorption and ultraviolet photoelectron spectroscopy (UPS) spectra (Fig. S9), the valence band maximum (E_V), Fermi level (E_F), and conduction band minimum (E_C) of the $MAPbBr_3/MAPbI_3$ heterojunction were calculated. The energy band diagram of the $MAPbBr_3/MAPbI_3$ photodetector is depicted in Fig. 4a, which forms a type-II heterojunction. This band structure creates a built-in electric field at the interface, which facilitates the efficient separation and transport of photogenerated electron–hole pairs, enabling the device operation at zero bias. This built-in electric field has been confirmed by the accelerated carrier extraction observed in TRPL (Fig. S10) and the distinct surface potential difference directly mapped via Kelvin probe force microscopy (KPFM) (Fig. S11). The current density–voltage (*J-V*) curves of the self-powered photodetector array under dark condition and 532 nm illumination with light intensity varying from 66 nW cm^{-2} to 1.291 mW cm^{-2} are

https://doi.org/10.1007/s40820-026-02224-6

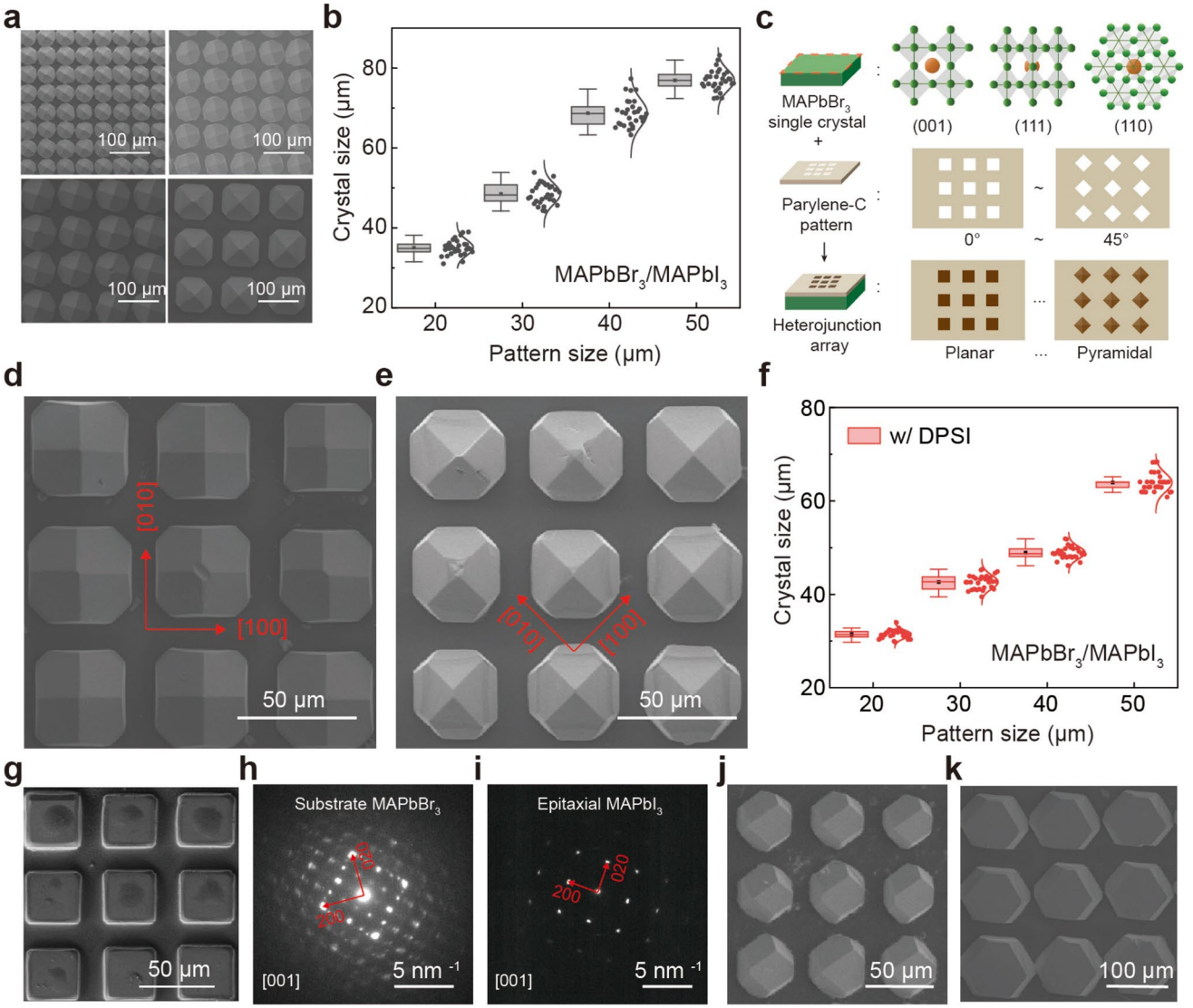

Fig. 3 Controllable epitaxial growth of $MAPbBr_3/MAPbI_3$ perovskite single-crystal heterojunction arrays. **a** SEM images of selective epitaxial $MAPbI_3$ single-crystal arrays with varying sizes. **b** Dependence of pixel size on template opening size for $MAPbI_3$ single-crystal arrays epitaxially grown on $MAPbBr_3$ substrates. **c** Schematic diagram of precise adjustment of pixel arrangement angle and crystal orientation by tuning the angle between pattern opening and substrate crystal orientation. SEM images of epitaxial $MAPbI_3$ single-crystal arrays with different angles of **d** 0° and **e** 45°. **f** Pixel size versus template opening size for epitaxial $MAPbI_3$ single-crystal arrays with the addition of DPSI to the $MAPbBr_3$ precursor solution. **g** SEM image of epitaxial $MAPbI_3$ perovskite single-crystal arrays with DPSI. **h** SAED patterns of the $MAPbBr_3$ substrate. **i** SAED patterns of the corresponding epitaxial $MAPbI_3$ perovskite single-crystal arrays with DPSI. SEM images of epitaxial $MAPbI_3$ perovskite single-crystal arrays with different crystal orientations of **j** (111) and **k** (110)

shown in Fig. 4b. The normalized responsivity of the self-powered photodetector array under full spectrum is also characterized in the Fig. S12. Figure 4c shows the current density-time (*J*-*t*) characteristics of the device under 0 V bias. The device demonstrates stable and repeatable on/off switching behaviors across a wide range of light intensities. Importantly, the device maintains a stable photoresponse at an ultralow light intensity of 9 nW cm^{-2} (Fig. S13), demonstrating high sensitivity and a detection limit competitive with previously reported perovskite heterojunction photodetectors (Table S1). Responsivity under different illuminations is a key metric for assessing detector performance. Figure 4d plots the photocurrent density and responsivity as functions of light intensity. The photocurrent shows a linear

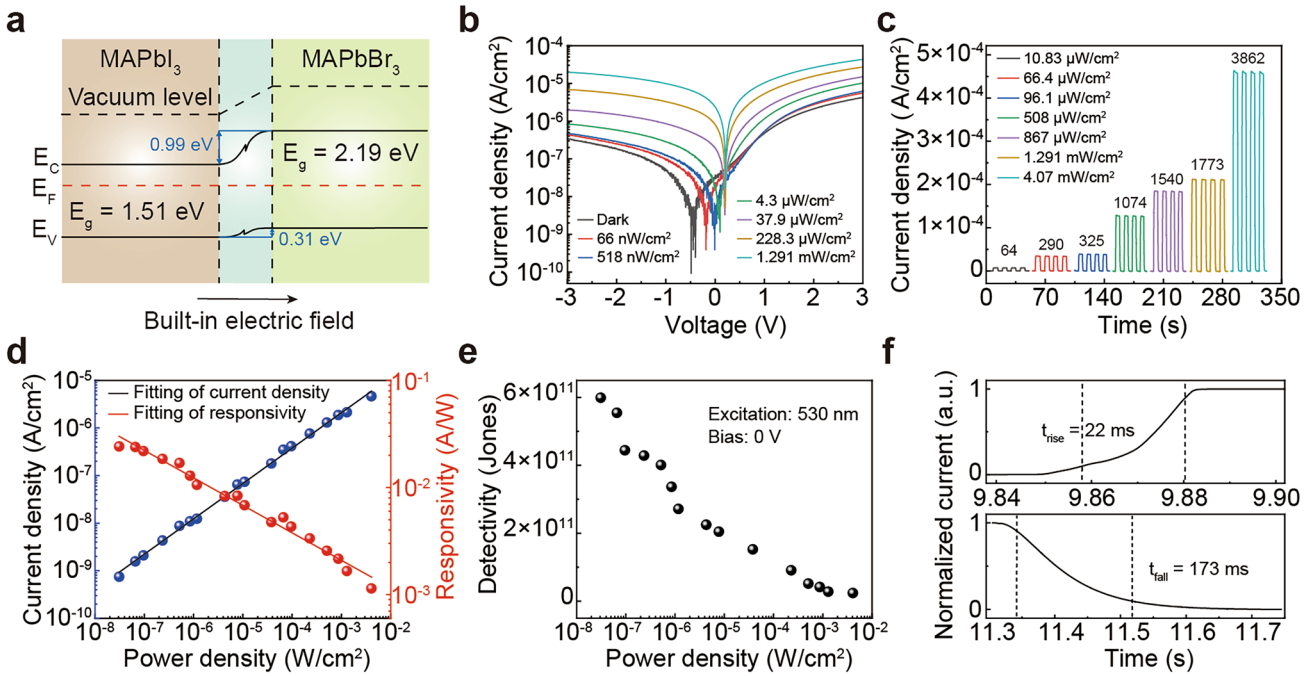

Fig. 4 Optoelectronic response of the self-powered photodetector array based on $MAPbBr_3/MAPbI_3$ perovskite single-crystal heterojunction array. **a** Energy band diagram of the self-powered photodetector. **b** *J-V* characteristics under varying light intensities. **c** Current density of the device under different light irradiation. The specific value of the on–off ratio of the device is labeled on the curve. **d** Photocurrent density and responsivity under different light intensities. **e** Specific detectivity under different light intensities. **f** Response time of the self-powered photodetector array

dependence on the light intensity and the responsivity is higher at lower light intensities, exhibiting a peak responsivity of 2.4 mA W^{-1}. The specific detectivity (D^*) is plotted with the light intensity, reaching 6.0×10^{11} Jones under weak light conditions (Fig. 4e). The response time is defined as the time used for the current to switch between the 10% and 90% of its peak value. As shown in Fig. 4f, the self-powered photodetector array exhibits a fast response, with a rise time (t_{rise}) of 22 ms and a fall time (t_{fall}) of 173 ms. Furthermore, the device exhibits excellent operational stability, exhibiting a 10% decay in photocurrent after 7000 s of continuous on/off switching (Fig. S14a-d). Long-term stability was also evaluated by measuring the optoelectronic response after storage in ambient air for four weeks without encapsulation. As shown in Fig. S14e and f, the device retains stable switching behavior during the four weeks of ambient exposure, exhibiting a 10% degradation over this extended period. The optoelectronic performance of the self-powered photodetector arrays based on the $MAPbCl_3/MAPbBr_3$ heterojunction is summarized in Fig. S15. These results demonstrate that epitaxially grown single-crystal heterojunction arrays serve as a promising structure for the self-powered photodetectors. While the optoelectronic anisotropy of bulk perovskite single crystals has been investigated [54–60], establishing a systematic quantitative correlation between specific crystal orientations (e.g., (100), (110), (111)) and device performance remains challenging in these heterojunction arrays due to geometric and electrode contact constraints, which could be an important direction for future structure–property relationship investigations.

We further investigated the imaging capability of the 8 × 8 self-powered photodetector array. The imaging process is shown in Fig. 5a. In this setup, a light source projects an optical pattern through a mask onto the 8 × 8 device array, and an image is reconstructed by mapping the individual photocurrent response of each pixel. High pixel-to-pixel uniformity in both dark and illuminated conditions is important for the imaging applications. We first evaluated the dark current distribution across all 64 pixels. As shown in Fig. 5b, the dark current of all the pixels exhibits a concentrated distribution with a low average dark current of 32.96 ± 14.17 pA. Figure 5c demonstrates photocurrent distribution under various light intensities. With the light

https://doi.org/10.1007/s40820-026-02224-6

intensity increasing, the photocurrents of pixels enhanced accordingly while maintaining a narrow distribution, indicating a consistent and uniform photoresponse across the entire array. The ability to spatially resolve light patterns with minimal electrical crosstalk is also critical for a photodetector array. We selectively illuminated the central six pixels (pixels 34–39) of a single row while keeping the adjacent pixels (pixel 33 and 40) in the dark. As shown in Figs. 5d and S16, the currents of the illuminated pixels increase obviously with light intensity, while the currents of the dark pixel 33 and pixel 40 remaining unchanged. This result confirms that crosstalk between adjacent pixels is negligible, despite using the discrete heterojunction arrays on the continuous substrate. An 'H'-shaped light pattern was then projected onto the photodetector array. Figure 5e shows the resulting two-dimensional photocurrent maps recorded at different light intensities. As the light intensity increases, the 'H' pattern becomes clear. Specifically, as the illumination intensity gradually increases from 0 to 1.291 mW cm^{-2}, the photocurrent mapping of the input pattern exhibits a continuous multi-level response. Furthermore, to evaluate the imaging capabilities under complex scenarios, we scaled up

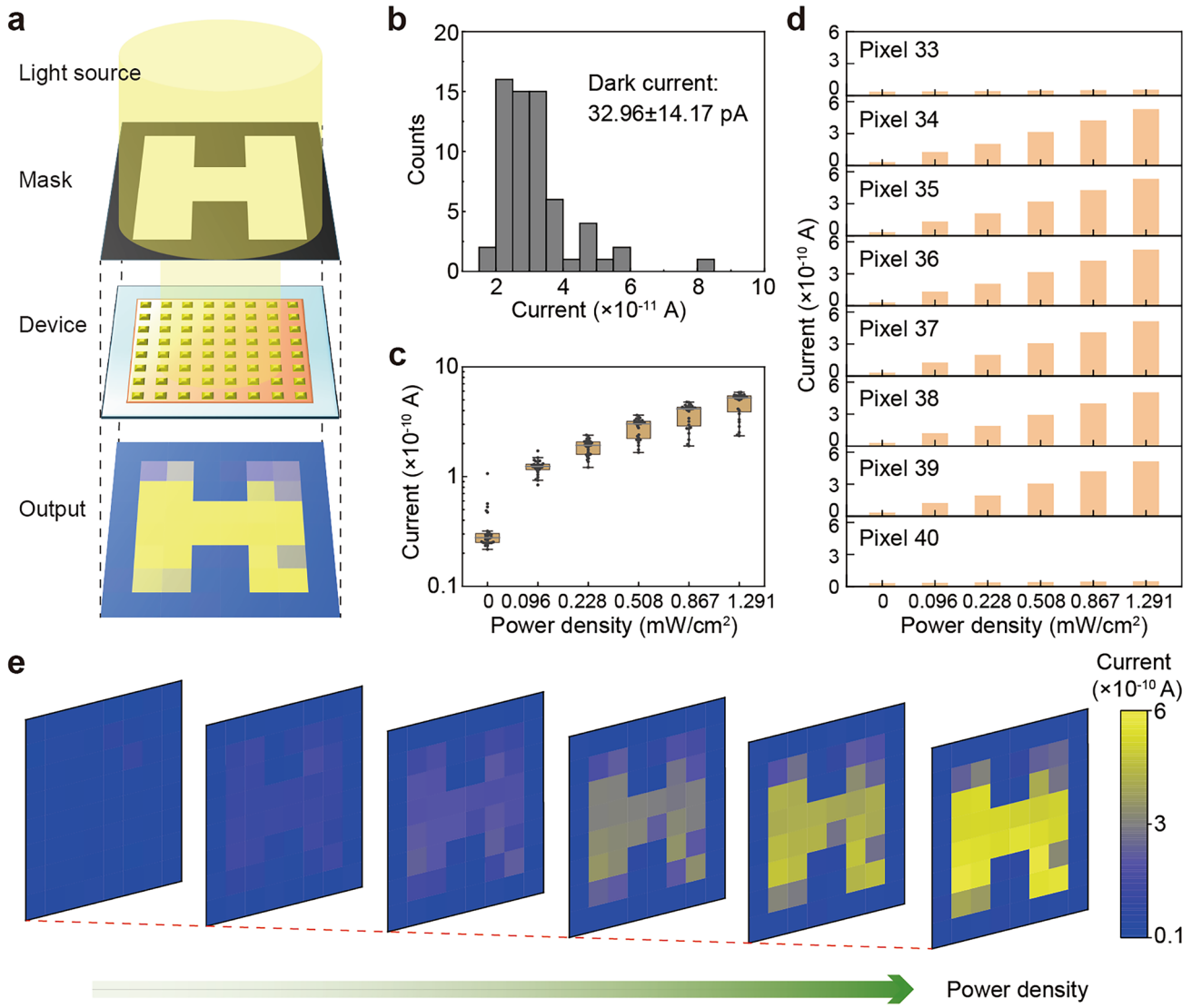

Fig. 5 Imaging applications of the self-powered photodetector array based on $MAPbBr_3/MAPbI_3$ perovskite single-crystal heterojunction array. **a** Schematic of the imaging process using the self-powered photodetector array. **b** Statistical distribution of dark current for all 64 pixels within the 8×8 array. **c** Statistical distribution of photocurrent for all 64 pixels under illumination at different light intensities. **d** Output current of eight pixels (Pixels 33–40) along the fifth row of the array device under varying light intensities. **e** Photocurrent mapping of the 8×8 array acquired under the different light intensities

the device to a 16 × 16 $MAPbBr_3$/$MAPbI_3$ perovskite single-crystal heterojunction array (Fig. S17). A "Christmas tree" pattern was projected onto the array. The photocurrent mapping accurately reconstructed the sharp geometric outlines and spatial features of the pattern. By extracting the modulation transfer function (MTF), the device demonstrated a spatial resolution of 8.0 lp mm^{-1} at an MTF of 0.2, confirming the capability for resolving fine optical details.

4 Conclusions

In summary, we demonstrated a simple and versatile strategy for the fabrication of orientation-controlled single-crystal perovskite heterojunction arrays. By combining the patterned Parylene-C film for spatial confinement with the single-crystal substrate for epitaxial guidance, this method demonstrated the precise control over the geometric parameters and crystallographic properties of the array. The resulting $MAPbCl_3$/$MAPbBr_3$ and $MAPbBr_3$/$MAPbI_3$ heterojunction arrays exhibited high crystal quality and uniformity, which enabled high sensitivity and imaging capability of the corresponding self-powered photodetector arrays based on these heterojunctions.

Acknowledgements The authors thank the support of National Natural Science Foundation of China (No. 52125205, 52532005 and 52250398), the Fundamental Research Funds for the Central Universities and the Postdoctoral Fellowship Program of CPSF (Grant No. GZC20252686) for their support. The authors also thank Xuzhou B&C Chemical Co. Ltd for providing the photoresist (HTA116, HTA112, B&C Chemicals) used in our work.

Author contributions W.W., X.H., and C.P. jointly conceived and supervised the project. Y.Y. designed and fabricated the perovskite single-crystal heterojunction self-powered photodetector arrays. H.L. and Y.Y. characterized the performance of perovskite single-crystal heterojunction arrays and completed imaging tests of the self-powered photodetector array device. H.L., Y.Y. and X.H. wrote the manuscript. All authors discussed the results and commented on the manuscript.

Declarations

Conflict of interest The authors declare no interest conflict. They have no known competing financial interests or personal relationships that could have appeared to influence the work reported in this paper.

Supplementary Information The online version contains supplementary material available at https://doi.org/10.1007/s40820-026-02224-6.

References

1. L. Zhang, M. Zhang, H. Wang, Z. Li, Z. Zhang et al., Diverse perovskite solar cells: progress, challenges, and perspectives. Adv. Mater. **38**(1), e12221 (2026). https://doi.org/10.1002/adma.202512221
2. S. Jia, C. Gu, X. Zhou, Y. Miao, Y. Tian et al., Self-assembled monolayers for high-performance perovskite solar cells. Adv. Funct. Mater. **36**(12), e12747 (2026). https://doi.org/10.1002/adfm.202512747
3. S.A. Ali Shah, M.H. Sayyad, Z. Guo, Light-emitting perovskite solar cells: genesis to recent drifts. Solar RRL **8**(23), 2400652 (2024). https://doi.org/10.1002/solr.202400652
4. Y.-H. Lin, Vikram, F. Yang, X.-L. Cao, A. Dasgupta et al., Bandgap-universal passivation enables stable perovskite solar cells with low photovoltage loss. Science **384**(6697), 767–775 (2024). https://doi.org/10.1126/science.ado2302
5. D. Gao, B. Li, Q. Liu, C. Zhang, Z. Yu et al., Long-term stability in perovskite solar cells through atomic layer deposition of tin oxide. Sci **386**(6718), 187–192 (2024). https://doi.org/10.1126/science.adq8385
6. Q. Zhou, G. Huang, J. Wang, T. Miao, R. Chen et al., Aromatic interaction-driven out-of-plane orientation for inverted perovskite solar cells with improved efficiency. Nat. Energy **10**(11), 1371–1381 (2025). https://doi.org/10.1038/s41560-025-01882-x
7. Y. Li, X. Guan, Y. Zhao, Q. Zhang, X. Chen et al., Modulation of charge transport layer for perovskite light-emitting diodes. Adv. Mater. **37**(25), 2410535 (2025). https://doi.org/10.1002/adma.202410535
8. H. Liu, G. Shi, C. Peng, W. Chen, H. Yao et al., Advances and challenges in large-area perovskite light-emitting diodes. Adv. Mater. **37**(25), e2410154 (2025). https://doi.org/10.1002/adma.202410154
9. Y. Deng, J. Liu, W. Liu, Y. Zhang, H. Gao et al., Buried interface modification for high-performance perovskite light-emitting diodes. Adv. Opt. Mater. **13**(26), e00894 (2025). https://doi.org/10.1002/adom.202500894

10. S. Zheng, Z. Wang, N. Jiang, H. Huang, X. Wu et al., Ultralow voltage–driven efficient and stable perovskite light-emitting diodes. Sci. Adv. **10**(36), eadp8473 (2024). https://doi.org/10.1126/sciadv.adp8473
11. Q. Zhang, K. Yang, C. Luo, Z. Lin, W. Chen et al., Nanosecond response perovskite quantum dot light-emitting diodes with ultra-high resolution for active display application. Light Sci. Appl. **14**(1), 285 (2025). https://doi.org/10.1038/s41377-025-01959-y
12. Y. Sun, L. Ge, L. Dai, C. Cho, J. Ferrer Orri et al., Bright and stable perovskite light-emitting diodes in the near-infrared range. Nat. **615**(7954), 830–835 (2023). https://doi.org/10.1038/s41586-023-05792-4
13. Z. Xu, X. Han, W. Wu, F. Li, R. Wang et al., Controlled on-chip fabrication of large-scale perovskite single crystal arrays for high-performance laser and photodetector integration. Light Sci. Appl. **12**(1), 67 (2023). https://doi.org/10.1038/s41377-023-01107-4
14. J. Meng, Q. Li, J. Huang, C. Pan, Z. Li, Self-powered photodetector for ultralow power density UV sensing. Nano Today **43**, 101399 (2022). https://doi.org/10.1016/j.nantod.2022.101399
15. W. Wu, H. Lu, X. Han, C. Wang, Z. Xu et al., Recent progress on wavelength-selective perovskite photodetectors for image sensing. Small Methods **7**(4), e2201499 (2023). https://doi.org/10.1002/smtd.202201499
16. W. Wang, W. Tian, F. Chen, J. Wang, W. Zhai et al., Filter-less color-selective photodetector derived from integration of parallel perovskite photoelectric response units. Adv. Mater. **36**(33), 2404968 (2024). https://doi.org/10.1002/adma.202404968
17. Z. Zhu, H. Chen, W. Huang, B. Zhao, S. Gao et al., Ion leakage current control for polycrystalline metal halide perovskite direct X-ray detectors. ACS Appl. Mater. Interfaces **16**(39), 53177–53185 (2024). https://doi.org/10.1021/acsami.4c10707
18. L. Min, H. Sun, L. Guo, M. Wang, F. Cao et al., Frequency-selective perovskite photodetector for anti-interference optical communications. Nat. Commun. **15**(1), 2066 (2024). https://doi.org/10.1038/s41467-024-46468-5
19. X. Han, J. Tao, Y. Liang, F. Guo, Z. Xu et al., Ultraweak light-modulated heterostructure with bidirectional photoresponse for static and dynamic image perception. Nat. Commun. **15**(1), 10430 (2024). https://doi.org/10.1038/s41467-024-54845-3
20. Z. He, B. Sun, H. Lu, X. Sun, Z. Xu et al., Focus-tunable real-time imaging system based on ultrathin perovskite curved image sensor with hierarchical mesh design. Sci. Adv. **11**(36), eadw7826 (2025). https://doi.org/10.1126/sciadv.adw7826
21. T.M.H. Nguyen, S.G. Shin, H.W. Choi, C.W. Bark, Recent advances in self-powered and flexible UVC photodetectors. Explor. **2**(5), 20210078 (2022). https://doi.org/10.1002/EXP.20210078
22. X. Cao, S. Xing, R. Lai, Y. Lian, Y. Wang et al., Low-threshold, external-cavity-free flexible perovskite lasers. Adv. Funct. Mater. **33**(19), 2211841 (2023). https://doi.org/10.1002/adfm.202211841
23. J. Moon, Y. Mehta, K. Gundogdu, F. So, Q. Gu, Metal-halide perovskite lasers: cavity formation and emission characteristics. Adv. Mater. **36**(20), 2211284 (2024). https://doi.org/10.1002/adma.202211284
24. Y. Li, S. Liu, T. Feeney, J. Roger, M. Gholipoor et al., Electrically-switchable gain in optically pumped $CsPbBr_3$ lasers with low threshold at nanosecond pumping. Small **21**(13), 2411935 (2025). https://doi.org/10.1002/smll.202411935
25. C. Zou, X. Cao, Z. Wang, Y. Yang, Y. Lian et al., Continuous-wave perovskite polariton lasers. Sci. Adv. **11**(2), eadr8826 (2025). https://doi.org/10.1126/sciadv.adr8826
26. X. Li, Y. Jia, M. Liu, S. He, J. Guo et al., Ultrastable lasing from perovskite colloidal nanocrystals. Sci. Adv. **11**(28), eadq9002 (2025). https://doi.org/10.1126/sciadv.adq9002
27. C. Ge, Y. Li, H. Song, Q. Xie, L. Zhang et al., Anisotropic carrier dynamics and laser-fabricated luminescent patterns on oriented single-crystal perovskite wafers. Nat. Commun. **15**(1), 914 (2024). https://doi.org/10.1038/s41467-024-45055-y
28. G. Vats, B. Hodges, A.J. Ferguson, L.M. Wheeler, J.L. Blackburn, Optical memory, switching, and neuromorphic functionality in metal halide perovskite materials and devices. Adv. Mater. **35**(37), 2205459 (2023). https://doi.org/10.1002/adma.202205459
29. S. Liu, P. Li, X. Fu, K. Zhou, Y. Ji et al., Ionic behaviors of perovskite devices and their neuromorphic applications. Adv. Funct. Mater. **36**(15), e10934 (2026). https://doi.org/10.1002/adfm.202510934
30. T. Liu, H. Wang, C. Sun, Z. Yuan, X. Wang et al., Suppression of tin oxidation *via* Sn→B bonding interactions for high-resolution lead-free perovskite neuromorphic imaging sensors. Adv. Mater. **37**(29), 2502015 (2025). https://doi.org/10.1002/adma.202502015
31. R.A. John, A. Milozzi, S. Tsarev, R. Brönnimann, S.C. Boehme et al., Ionic-electronic halide perovskite memdiodes enabling neuromorphic computing with a second-order complexity. Sci. Adv. **8**(51), eade0072 (2022). https://doi.org/10.1126/sciadv.ade0072
32. H. Wang, B. Sun, S.S. Ge, J. Su, M.L. Jin, On non-von Neumann flexible neuromorphic vision sensors. npj Flex. Electron. **8**, 28 (2024). https://doi.org/10.1038/s41528-024-00313-3
33. Z. Yang, S. Huo, Z. Zhang, F. Meng, B. Liu et al., High-precision multibit opto-electronic synapses based on ReS_2/h-BN/graphene heterostructure for energy-efficient and high-accuracy neuromorphic computing. Adv. Funct. Mater. **35**(48), 2509119 (2025). https://doi.org/10.1002/adfm.202509119
34. F. Guo, X. Yang, P. Wang, X. Bai, T. Kong et al., Advances in single-crystal films: Synergistic insights from perovskites and organic molecules for high-performance optoelectronics. Small **21**(19), 2412101 (2025). https://doi.org/10.1002/smll.202412101
35. W. Wu, X. Han, J. Li, X. Wang, Y. Zhang et al., Ultrathin and conformable lead halide perovskite photodetector arrays for potential application in retina-like vision sensing. Adv. Mater. **33**(9), 2006006 (2021). https://doi.org/10.1002/adma.202006006
36. Q. Wang, G. Zhang, H. Zhang, Y. Duan, Z. Yin et al., High-resolution, flexible, and full-color perovskite image photodetector *via* electrohydrodynamic printing of ionic-liquid-based

ink. Adv. Funct. Mater. **31**(28), 2100857 (2021). https://doi.org/10.1002/adfm.202100857

37. Y. Chen, C. Zhao, T. Zhang, X. Wu, W. Zhang et al., Flexible and filter-free color-imaging sensors with multicomponent perovskites deposited using enhanced vapor technology. Small **17**(26), 2007543 (2021). https://doi.org/10.1002/smll.202007543
38. B. Peng, H. Zhou, Z. Liu, Y. Li, Q. Shang et al., Pattern-selective molecular epitaxial growth of single-crystalline perovskite arrays toward ultrasensitive and ultrafast photodetector. Nano Lett. **22**(7), 2948–2955 (2022). https://doi.org/10.1021/acs.nanolett.2c00074
39. Y. Hou, J. Li, J. Yoon, A.M. Knoepfel, D. Yang et al., Retina-inspired narrowband perovskite sensor array for panchromatic imaging. Sci. Adv. **9**(15), eade2338 (2023). https://doi.org/10.1126/sciadv.ade2338
40. Z. Long, X. Qiu, C.L.J. Chan, Z. Sun, Z. Yuan et al., A neuromorphic bionic eye with filter-free color vision using hemispherical perovskite nanowire array retina. Nat. Commun. **14**(1), 1972 (2023). https://doi.org/10.1038/s41467-023-37581-y
41. Y. Zhou, D. Liu, H.G. Yang, S. Yang, Y. Hou, Preparation techniques for perovskite single crystal films: from nucleation to growth. Chem. **20**(4), e202401294 (2025). https://doi.org/10.1002/asia.202401294
42. Y. Pan, X. Wang, Y. Liao, Y. Xu, Y. Li et al., Epitaxial perovskite single-crystalline heterojunctions for filter-free ultra-narrowband detection with tunable spectral responses. ACS Appl. Mater. Interfaces **14**(44), 50331–50342 (2022). https://doi.org/10.1021/acsami.2c13126
43. Y. He, S. Gao, B. Zhao, H. Chen, Z. Zhu et al., Epitaxial growth of high-quality perovskite heterojunctions for direct-conversion X-ray detectors. ACS Energy Lett. **10**(6), 2770–2777 (2025). https://doi.org/10.1021/acsenergylett.5c00938
44. Y. Guan, C. Zhang, Z. Liu, Y. Zhao, A. Ren et al., Single-crystalline perovskite p–n junction nanowire arrays for ultrasensitive photodetection. Adv. Mater. **34**(35), 2203201 (2022). https://doi.org/10.1002/adma.202203201
45. J. Zhang, C. Li, Y. Liang, J. Song, Q. Shang et al., Solution-processed selective area homoepitaxial growth of suspended $MAPbX_3$ (X = Cl, Br) perovskite micro-arrays. Adv. Funct. Mater. **33**(4), 2208841 (2023). https://doi.org/10.1002/adfm.202208841
46. J. Yan, F. Gao, Y. Tian, Y. Li, W. Gong et al., Controllable perovskite single crystal heterojunction for stable self-powered photo-imaging and X-ray detection. Adv. Opt. Mater. **10**(17), 2200449 (2022). https://doi.org/10.1002/adom.202200449
47. Y. Peng, J. Lu, X. Wang, W. Ma, M. Que et al., Self-powered high-performance flexible GaN/ZnO heterostructure UV photodetectors with piezo-phototronic effect enhanced photoresponse. Nano Energy **94**, 106945 (2022). https://doi.org/10.1016/j.nanoen.2022.106945
48. Y. Chen, X. Peng, W. Qin, S. Li, L. Zhang et al., Filterless bandpass photodetectors enabled by 2D/3D perovskite heterojunctions. Adv. Funct. Mater. **34**(41), 2403942 (2024). https://doi.org/10.1002/adfm.202403942
49. Z. Guo, J. Zhang, X. Liu, L. Wang, L. Xiong et al., Optoelectronic synapses and photodetectors based on organic semiconductor/halide perovskite heterojunctions: materials, devices, and applications. Adv. Funct. Mater. **33**(46), 2305508 (2023). https://doi.org/10.1002/adfm.202305508
50. J. Hao, Y.-H. Kim, S.N. Habisreutinger, S.P. Harvey, E.M. Miller et al., Low-energy room-temperature optical switching in mixed-dimensionality nanoscale perovskite heterojunctions. Sci. Adv. **7**(18), eabf1959 (2021). https://doi.org/10.1126/sciadv.abf1959
51. X. Li, W. Zhang, X. Guo, C. Lu, J. Wei et al., Constructing heterojunctions by surface sulfidation for efficient inverted perovskite solar cells. Sci. **375**(6579), 434–437 (2022). https://doi.org/10.1126/science.abl5676
52. D. Liu, J. Bi, W. Xu, K.W.P. Orr, F. Wang et al., Strain relaxation in halide perovskites *via* 2D/3D perovskite heterojunction formation. Sci. Adv. **11**(26), eadu3459 (2025). https://doi.org/10.1126/sciadv.adu3459
53. B. Li, Q. Liu, J. Gong, S. Li, C. Zhang et al., Harnessing strong aromatic conjugation in low-dimensional perovskite heterojunctions for high-performance photovoltaic devices. Nat. Commun. **15**(1), 2753 (2024). https://doi.org/10.1038/s41467-024-47112-y
54. L. Zhang, S. Cui, Q. Guo, C. Ge, Q. Han et al., Anisotropic performance of high-quality $MAPbBr_3$ single-crystal wafers. ACS Appl. Mater. Interfaces **12**(46), 51616–51627 (2020). https://doi.org/10.1021/acsami.0c14582
55. P. Zhang, G. Zhang, L. Liu, D. Ju, L. Zhang et al., Anisotropic optoelectronic properties of melt-grown bulk $CsPbBr_3$ single crystal. J. Phys. Chem. Lett. **9**(17), 5040–5046 (2018). https://doi.org/10.1021/acs.jpclett.8b01945
56. P. Saha, M.M. Rahman, C.L. Tolbert, C.M. Hill, Facet-dependent photoelectrochemistry on single crystal organic-inorganic halide perovskite electrodes. Chem. Biomed. Imaging **1**(5), 488–494 (2023). https://doi.org/10.1021/cbmi.3c00069
57. S. Dong, Z.-Y. Hu, P. Wei, J. Han, Z. Wang et al., All-inorganic perovskite single-crystal photoelectric anisotropy. Adv. Mater. **34**(37), 2204342 (2022). https://doi.org/10.1002/adma.202204342
58. Z.Y. Zhang, G.P. Wang, High-performance photoconductive unidirectional rectification in perovskite single-crystal. Adv. Opt. Mater. **14**(10), e03555 (2026). https://doi.org/10.1002/adom.202503555
59. X. Cheng, L. Jing, Y. Zhao, S. Du, J. Ding et al., Crystal orientation-dependent optoelectronic properties of $MAPbCl_3$ single crystals. J. Mater. Chem. C **6**(6), 1579–1586 (2018). https://doi.org/10.1039/c7tc05156e
60. N.K. Tailor, S. Satapathi, Anisotropy in perovskite single crystals: from fundamentals to applications. J. Phys. Chem. C **126**(42), 17789–17803 (2022). https://doi.org/10.1021/acs.jpcc.2c05534

 https://doi.org/10.1007/s40820-026-02224-6